Ebola and Marburg virus matrix layers are locally ordered assemblies of VP40 dimers

Authors:

Wan, W.[1,2,#], Clarke, M.[1], Norris, M.[3], Kolesnikova, L.[4], Koehler, A.[4], Bornholdt, Z.[5,##], Becker, S.[4], Saphire E.O.[3] and Briggs, J.A.G.[1,6]

1 Structural and Computational Biology Unit, European Molecular Biology Laboratory, Meyerhofstrasse 1, 69117 Heidelberg, Germany

2 Department of Molecular Structural Biology, Max Planck Institute of Biochemistry, Am Klopferspitz 18, 82152 Martinsried, Germany

3 Center for Infectious Disease and Vaccine Research, La Jolla Institute for Immunology, La Jolla, CA 92037

4 Institut für Virologie, Philipps-Universität Marburg, Hans-Meerwein-Straße, 35043 Marburg, Germany.

5 The Scripps Research Institute, La Jolla, CA 92037

6 Structural Studies Division, MRC Laboratory of Molecular Biology, Francis Crick Avenue, Cambridge CB2 0QH, UK

present address: Department of Biochemistry and Center for Structural Biology
Vanderbilt University, Nashville, TN, USA

present address: Mapp Biopharmaceutical, San Diego, CA 92121

* correspondence to JAGB: john.briggs@mrc-lmb.cam.ac.uk

Abstract:

A key step in the life cycle of enveloped viruses is the budding of nascent virions from the host membrane. In filoviruses such as Ebola and Marburg virus, this process is achieved by the matrix protein VP40. When expressed alone, VP40 induces the budding of filamentous virus-like particles, suggesting that localization to the plasma membrane, oligomerization into a matrix layer, and the generation of membrane curvature are intrinsic properties of VP40. While a number of crystal structures of VP40 have been determined in various oligomerization states, there has been no direct information on the structure of assembled VP40 matrix layers within viruses or virus-like particles. Here, we present structures of Ebola and Marburg VP40 matrix layers in intact virus-like particles, as well as within intact Marburg viruses. We find that the matrix layers are formed from VP40 dimers which assemble into extended chains via C-terminal domain interactions. These chains stack into layers, forming a 2D lattice below the membrane surface. However, these 2D lattices are only locally ordered, forming a patchwork assembly across the membrane surfaces and suggesting that assembly may begin at multiple points. These observations define the structure and arrangement of the matrix protein layer that mediates the formation of filamentous filovirus particles.

Introduction

The filovirus family includes viruses such as Ebola, Marburg and Sudan viruses that can cause hemorrhagic fever and severe disease (Feldmann et al., 2013). Filoviruses package their single-stranded negative-sense RNA genomes with viral proteins including nucleoprotein (NP), VP24 and VP35, into helical ribonucleoprotein assemblies called nucleocapsids (NCs) (Huang et al., 2002; Noda et al., 2010; Wan et al., 2017). NCs are recruited to the plasma membrane and bud from the host cells as enveloped virions with a characteristic filamentous morphology from which the family takes its name(Geisbert and Jahrling, 1995).

The filovirus matrix protein, VP40, binds to and concentrates at the plasma membrane of infected cells, where it can interact with components of the NC to promote envelopment, and where it drives formation of the filamentous virus particles. VP40 is required for viral budding, and expression of VP40 alone is sufficient to drive formation of filamentous virus-like particles (VLPs) containing a matrix layer and membrane envelope (Harty et al., 2000; Jasenosky et al., 2001; Noda et al., 2002; Timmins et al., 2001). The morphology of these VLPs is similar to that of true virions but their diameter is smaller (Noda et al., 2002). When VP40 is co-expressed with NC components NP, VP24 and VP35, VLPs are produced which are almost indistinguishable from true virions(Bharat et al., 2012; Noda et al., 2005; Wan et al., 2017).

A number of crystal structures have been determined of Ebola virus VP40 (eVP40) and Sudan (Ebola) virus (sVP40) (Bornholdt et al., 2013; Clifton et al., 2015; Dessen et al., 2000; Gomis-Rüth et al., 2003). VP40 contains an N-terminal

domain (NTD) and a C-terminal domain (CTD), linked by an intrasubunit hinge. Both eVP40 and sVP40 have been crystallized in space group C2 with similar unit cell dimensions. These crystals reveal dimers assembled via a hydrophobic interface in the NTD, involving residues A55, H61, F108, A113, M116, and L117 which are distributed across two alpha-helices (residues 52-65, 108-117). Disruption of the NTD dimer interface by site-directed mutagenesis prevents migration of VP40 to the plasma membrane and prevents matrix assembly(Bornholdt et al., 2013). Within the typical C2 crystal packing of unmodified VP40, eVP40 and sVP40 dimers are further arranged in linear assemblies via a hydrophobic CTD-CTD interface(Bornholdt et al., 2013; Dessen et al., 2000) (**Fig. S1a,b**). This interface involves residues L203, I237, M241, M305, and I307, which together form a relatively smooth hydrophobic patch (**Fig. S1a**). The CTD also contains a basic patch composed of six lysine residues (K221, K224, K225, K270,K274, K275), which is essential for matrix assembly and membrane budding (**Fig. S1a**).

A crystal structure of Marburg VP40 (mVP40) has also been determined(Oda et al., 2016) (**Fig. S1c**). eVP40 and mVP40 have 42% sequence identity and a C-alpha RMSD of 2.4 Å in the NTD, but only 16% sequence identity and 5.6 Å C-alpha RMSD in the CTD. The overall topology of mVP40, however, is similar to that of eVP40. The mVP40 monomer has similar N- and C-terminal domains, although there is a small rotation of the CTD relative to the NTD when compared to eVP40. mVP40 dimerizes via an NTD interface that is very similar to that in eVP40, and mVP40 also forms dimers in solution that are required for membrane binding and filament budding. The mVP40 CTD basic patch is also required for membrane binding but is larger and flatter than that in eVP40. In the mVP40 crystal packing, the CTDs meet at an angle and do not form the more extensive hydrophobic interface observed in the C2 crystals of eVP40 and sVP40 (**Fig. S1**).

Deletion or proteolysis of the C-terminus or C-terminal domain or incubation with urea drives oligomerization of the eVP40 NTD into RNA-binding octameric rings(Bornholdt et al., 2013; Gomis-Rüth et al., 2003). Subsequent work suggests that octameric rings are likely to have a function during the viral lifecycle independent of matrix formation(Bornholdt et al., 2013; Gomis-Rüth et al., 2003; Hoenen et al., 2010b, 2005).

In an effort to mimic membrane-associated electrostatic conditions, a crystal structure of eVP40 was determined in the presence of the negatively charged additive dextran sulfate(Bornholdt et al., 2013). Under these conditions, eVP40 assembled into linear hexamers (**Fig. S1d**) with unit distances approximately consistent with earlier, lower resolution tomographic analysis of the VP40 layer in Ebola and Marburg virions(Beniac et al., 2012; Bharat et al., 2011). The core of the linear hexamer consists of four NTDs from which the linked CTDs are disordered or “sprung” and not resolved. The first and sixth VP40s in the hexamer retain their CTD in close association with its NTD. These CTDs assemble into linear filaments via the same CTD-CTD interactions observed in the C2 crystals of VP40 dimers. The NTD-NTD interfaces within the hexamer alternate between the dimer interface and the same NTD-NTD interface observed in the

octameric ring. No linear hexamer structure has been determined for mVP40. However, mutagenesis of residues in mVP40 homologous to those forming the "octamer-like" interfaces in hexameric eVP40 (Bornholdt et al., 2013; Hoenen et al., 2010a) retains the ability of mVP40 to dimerize but prevents membrane binding and budding. Based on existing data it seems likely that VP40 is arranged in a similar way in both MARV and EBOV particles.

The current model for the assembly state of VP40 within filovirus particles consists of VP40 hexamers as crystallized in the presence of dextran sulfate, arranged to form a 2D lattice, with dimensions of the 2D lattices in the model based upon repeating features observed in low-resolution cryo-electron tomography (cryo-ET) studies(Beniac et al., 2012; Bharat et al., 2011; Bornholdt et al., 2013). The structure and arrangement of VP40 within actual assembled virus particles, however, is unknown. It therefore remains unclear how VP40 assembles in the actual virion, which model of VP40 assembly best reflects that in the virion, and how VP40 induces membrane curvature and assembly with other viral components. Here we have set out to directly determine the structure and arrangement of VP40 within filamentous virus-like particles and authentic filovirus virions.

Results

The linear CTD-CTD interface is consistently observed in unmodified VP40 crystals

eVP40 and sVP40, with intact CTDs and in the absence of charged additives, consistently crystallize in linear filaments of dimers in the space group C2(Bornholdt et al., 2013; Clifton et al., 2015; Dessen et al., 2000). In an attempt to determine if this linear arrangement is an inherent preferred assembly interface of eVP40 or simply the result of the common C2 crystal packing, we crystallized eVP40 in two alternate crystal forms: $P6_2$ and $P6_422$. Notably, in both of these crystal forms, eVP40 also builds linear filaments of dimers, mediated by CTD-CTD interdimer interfaces, with CTD basic patches displayed on a common face. These filaments differ from the C2 filaments by slight torsional rotation about the relatively flat hydrophobic CTD-CTD interface (**Fig. S1e,f and Table S1**). The propensity of VP40 to form linear assemblies by CTD-CTD interactions across multiple crystal forms suggest this is a biologically preferred interface and may be important in the viral particle or virus assembly.

The structure of the matrix layer in EBOV VLPs

eVP40 expression induces budding of long VLPs from the surface of mammalian cells(Noda et al., 2002; Timmins et al., 2001). We purified Zaire eVP40 VLPs by sucrose gradient purification and imaged them by cryo-ET, finding multi-micron long filaments with a diameter of ~28 nm (**Table 1**) and a matrix-like protein layer visible under the membrane bilayer. We applied subtomogram averaging methods to determine the structure of the matrix layer to a resolution of 10 Å (**Fig. 1, Fig. S2**) from intact eVP40 VLPs. We observed that the matrix layer is formed by higher-order linear oligomerization of VP40 dimers on the inner surface of the viral membrane. VP40 dimers form long chains that stack to form 2D lattices with a monoclinic p2 space group in the plane of the membrane (**Fig. 1, Table 1**). The crystal structure of the C2 eVP40 dimer (PDB: 4LDB) could be

fit as a rigid body into the density, showing that linear oligomerization is mediated by CTD to CTD interactions.

In addition to eVP40 VLPs, we also produced VLPs by co-expression of eVP40 with the Ebola virus glycoprotein GP, and by co-expression of eVP40 with the NC components NP, VP24 and VP35. As described previously(Bharat et al., 2012), NP-VP24-VP35-VP40 VLPs have substantially wider filaments to accommodate the NC-like assembly (**Table 1**). We determined the structures of eVP40 within these VLPs at resolutions of 10 Å, (**Fig. 1, Fig. S2**). As in the eVP40 VLPs, the matrix layer in these VLPs is formed from extended chains of eVP40 that stack to form monoclinic p2 lattices (**Fig. 1, Table 1**).

EBOV matrix layer is formed by oligomerization of VP40 dimers into chains

We were able to fit the C2 crystallographic eVP40 dimer as a rigid body into the matrix structures from all three VLPs (**Fig. 1**). We did not observe any substantial electron density that is not occupied by eVP40. The eVP40 dimers are oriented similarly such that the basic patches in the CTDs all point towards and contact the membrane. This orientation is consistent with previous studies, which showed that mutations within this patch modulate membrane binding(Bornholdt et al., 2013), and consistent with linear assemblies observed in crystals in which the basic patches are oriented in the same direction.

In all VLPs, oligomerization of eVP40 dimers to form extended chains occurs through a hydrophobic surface patch in the CTD. A hydrophobic CTD-CTD interaction is also found in each of the C2, $P6_2$ and $P6_422$ eVP40 and sVP40 crystal forms, with slightly varying orientations about the CTD-CTD interface (**Fig. S1, S3**). In contrast to the flexible CTD-CTD interface, the dimeric NTD-NTD interfaces are considered rigid(Bornholdt et al., 2013), and are largely conserved in different crystal structures (**Fig. S3**). The flexibility about the CTD-CTD interfaces, and possibly also from the intrasubunit NTD-CTD hinge, appear sufficient to accommodate the varying radii of assembled matrix layers.

We previously probed the CTD-CTD interface by introducing either an M241R point mutation or an I307R mutation, both of which lie in the CTD-CTD interface. I307R was combined with R134A in the octameric assembly site to inhibit octamer formation. VP40 mutants bearing M241R or I307R substitutions do not assemble VLPs. We sought to identify an alternate mutation that would stabilize, instead of disrupt, the CTD-CTD interaction. We generated eVP40 bearing an M305F/I307F double mutation, which modeling studies suggested would support hydrophobic packing at the interface (**Fig. S4**). Although eVP40 M305F/I307F overall expressed to a lower yield, the relative proportion of VLP budding was enhanced over wild-type (**Fig. S4)**.

The structure of the matrix layer in MARV

In order to determine if the disparate sequence of the MARV VP40 CTD still resulted in a matrix assembly similar to that of eVP40, we prepared and purified mVP40 VLPs and determined the structure of the matrix layers to 10 Å resolution (**Fig. 2, Fig. S2**). The matrix layer appears similar to that seen in eVP40 VLPs, adopting a p2 lattice with similar dimensions (**Fig. 1, 2**), suggesting

that the structure is conserved despite sequence divergence (34% identical, 49% homologous). We fit the dimeric mVP40 crystal structure as well as a dimeric eVP40 crystal structure into the density as a rigid body. For mVP40 there were clashes of the CTDs at the inter-dimer interface (**Fig. S5**), while eVP40 fit these densities well. This suggests to us that the CTD of mVP40 is rotated slightly about the CTD-NTD hinge into a position more similar to that of eVP40 when assembled in VP40 VLPs.

We generated authentic MARV virions by infection of Huh7 cells and imaged fixed, purified virions by cryo-ET. MARV virion matrix layers again consist of VP40 dimers forming extended chains through their CTDs and stacking of these chains form a 2D p2 lattice (**Fig. 2**), but the lattice angles differ from those in VLPs: the VP40 chains run nearly perpendicular to the filament axis, and the register of neighboring chains differs by approximately half a VP40 protomer from those seen in VLPs (**Fig. 1, 2**). Rigid body fitting of mVP40 dimers or eVP40 dimers shows a good fit with no extra, unassigned densities (**Fig. 2**), suggesting that VP40 is the only component in the matrix layer. At this resolution we are unable to confidently assess whether the CTD has rotated slightly relative to the NTD or not.

We attempted to determine the structure of the matrix layer within authentic, fixed Ebola virions, but found that the some membranes were "moth-eaten", leaving membrane and matrix layers disrupted, while in others there were only few places where an ordered matrix layer was observed. We were therefore unable to determine a structure for VP40 within authentic EBOV virions.

Global Order of Filovirus Matrices

Lines of density that correspond to VP40 dimer chains are directly visible in tomograms of VLPs and viruses (**Fig. 3a**). General features such as the orientation of the chains relative to the axis of the filamentous particle are consistent with those determined by subtomogram averages.

When determining structures, subtomogram averaging provides the position and orientation of each VP40 dimer-centered subtomogram within the tomogram. Visualizations of these positions and orientations are called "lattice maps" and reveal the global arrangement of VP40 (**Fig. 3b,c**). Lattice maps show that in all VLPs studied, 2D lattices form locally ordered patches, and that there are disordered areas or other defects in crystallographic packing between the patches. The local pitch of the array is somewhat variable, and VP40 chains can terminate and run into each other. The overall topology of the matrix layer is a "patchwork" of locally ordered 2D lattices.

Based on the relative positions of subtomograms as visualized in the lattice maps, we calculated and plotted the average radius for each filamentous particle (at the matrix layer) against the pitch angle of the VP40 chains relative to the circumference of the VLP (**Fig. 4**). We find that despite the large differences in radius and angle, the radius of curvature of the VP40 chains is similar in all VLPs. Because we had not determined the structure, we did not derive these parameters for Ebola virions. Nevertheless, where small ordered regions of

VP40, or isolated VP40 chains were observed, they had a variable, but small angle relative to the filament, suggesting they have a radius of curvature similar to that observed in NP-VP24-VP35-VP40 VLPs (**Fig. S6**)

Spatial relationships between EBOV VP40 and other viral proteins

We next analyzed the spatial relationship between eVP40 and the other viral components NC or GP. To do this we first required the positions and orientations of the other viral components. For EBOV NP-VP24-VP35-VP40, NC positions had been calculated previously while determining the structure of the NC(Wan et al., 2017). For EBOV VP40-GP VLPs, we determined a low resolution structure of Ebola GP, thereby determining its position (**Fig. S7**). We then generated neighbor density maps: these show the relative distribution of all subtomograms of interest (those containing GP or NC) with respect to all reference subtomograms (those containing VP40) (**Fig. 5**).

We found that the NC layer is positioned at a consistent radial distance from VP40, but otherwise shows no defined spatial relationships with VP40 particles (**Fig. 5**). This arrangement is consistent with the presence of a tether (likely contributed by NP) that radially links VP40 and the NC layer. We estimated the stoichiometric ratio between VP40 and NC as ~4.4, suggesting that only a minority of VP40 molecules can be simultaneously bound by such a tether, and explaining the absence of any density corresponding to a bound tether in our VP40 structure.

We found that GP does not form an ordered lattice on the membrane. There is, however, a consistent radial distance between VP40 and nearby GP (**Fig. 5**); this distance is related to the thickness of the membrane envelope as is expected for proteins bound on opposite sides of the envelope. A tangential view of the neighbor plot shows weak striations in the GP layer, suggesting a tendency for GP to sit in preferred positions relative to the underlying VP40. We radially projected the GP neighbor positions onto the underlying VP40 lattice, revealing that GP is preferentially located at positions near the CTD-CTD interfaces of VP40.

Discussion

The previous model for the arrangement of VP40 within filoviruses was based upon a crystal structure obtained in the presence of dextran sulfate in which VP40 forms a hexamer. In this conformation, 6 VP40 NTDs form a linear oligomer, bracketed by a CTD on each end, with central CTDs “sprung” and therefore disordered on each side of the linear core (**Fig. S1**). In this model, the sprung CTDs protruding from one side of the NTD hexamer bind NC while those on the other side bind the plasma membrane. Higher-order oligomerization of hexamers via CTD interactions were then proposed to form a matrix lattice with dimensions similar to repeating features observed in cryo-electron tomograms (**Fig. 6**).

The VP40 matrix structures observed here in VLPs and virions reveal a linear arrangement of VP40 dimers without sprung CTDs. We suggest that the assembly of the half-sprung hexamer could have been the result of crystal packing and/or the presence of dextran sulfate. The interactions of the central VP40s in the hexamer are similar to those seen in the nucleic-acid binding octameric rings. It is possible that dextran sulfate is not acting as a membrane mimic, but instead as a nucleic acid mimic and inducing a conformation related to nucleic-acid binding octameric VP40 rings.

In all VP40 containing VLPs we studied, as well as in authentic MARV virions, the matrix layer is composed of linear chains of VP40 dimers, in which the dimeric interface is provided by the NTD, and the inter-dimer interface by the CTD. This linear arrangement of dimers is more similar to the packing of VP40 within C2 crystals and the $P6_2$ and $P6_422$ crystals presented here. In this arrangement, VP40 interacts with the membrane via basic patches in the CTD. VP40 chains are stacked to form 2D lattices on the underside of the viral membrane (**Fig. 6**).

The arrangement of VP40 which we observe provides a structural explanation for the phenotypes of a number of previously characterized EBOV and MARV VP40 mutants. Mutations in the basic patch which mediates the interaction between VP40 and the membrane, inhibit membrane binding, matrix assembly and budding for both eVP40(Bornholdt et al., 2013) and mVP40(Koehler et al., 2018). Mutations that disrupt the NTD-NTD dimeric interface prevent membrane binding, assembly, and budding for both eVP40(Bornholdt et al., 2013; Oda et al., 2016) and mVP40(Koehler et al., 2018), consistent with the key role of this interface in higher-order oligomerization of VP40. Mutations such as eVP40-M241R, which disrupts the hydrophobic patch of the CTD-CTD interface, lead to crystal forms which poorly recapitulate the CTD-CTD interface, while expression of eVP40 M241R or I307R block matrix assembly and budding(Bornholdt et al., 2013). Introduction of M305F/I307F instead of I307R, to enhance the hydrophobic interface, also enhances proportion of VLP release relative to expression level. Both mutants are consistent with a role for linear oligomerization of VP40 dimers via the hydrophobic CTD interface in promoting membrane curvature and filament growth(Bornholdt et al., 2013). Complete disruption of the CTD-CTD interface (eVP40-R134A/I307R) allows for membrane binding but not oligomerization, and neither budding nor ruffling is observed(Bornholdt et al., 2013).

The matrix layer we observe in both VLPs and in MARV virions has only local order. Patches of ordered VP40 are separated by various defects in the 2D crystallographic packing. It has been suggested that VP40 VLPs elongate perpendicularly from the plasma membrane(Kolesnikova et al., 2007b, 2007a). While it is possible to envisage filament protrusion as mediated by highly processive extension of VP40 chains at the base of an extending filament, our data are more consistent with assembly of the VP40 lattice from multiple starting points to generate a patchwork of locally ordered lattices at the assembly site. This mode of assembly is also easier to reconcile with our previous data suggesting that the budding of virions containing an NC takes place like a surfacing submarine, where the NC initially protrudes parallel to the

membrane surface before being wrapped from one end(Welsch et al., 2010). Because VP40 chains adopt preferred curvatures and therefore are oriented in a defined orientation relative to the membrane, neighboring patches would tend to agglomerate with their VP40 chains in approximately the same orientation.

We were unable to determine the structure of VP40 in Ebola virions, as the majority of viruses showed unstructured matrix layers. We think this is likely a fixation artefact, as Ebola virus preparations were generally more delicate than Marburg virus preparations. However, given our results with VLPs and the observations of ordered patches in some Ebola virions, we suggest that VP40 forms patchwork lattices of the same structure in Ebola virus.

We do not observe any substantial contribution to matrix density from another protein. However, given the ~4.4 VP40:NP ratio which we observed, we cannot rule out that a small part of every NP binds to one VP40 molecule, since the sub-stoichiometric levels of binding of a small additional density might not be detected.

GP has been previously shown to migrate towards VP40-rich membrane areas and colocalize with VP40 in VLPs(Licata et al., 2004; Noda et al., 2002). We observed that in EBOV VP40-GP VLPs, GP has a tendency to locate to striations that run perpendicular to the VP40 chains. These data suggest that GP preferentially sits at positions close to the inter-dimer CTD-CTD interfaces. Such a preferential localization could be derived through a direct interaction between VP40 CTD and the short, five-residue cytoplasmic tail of GP. Alternatively VP40 CTD may modify the local lipid composition to generate a local environment favorable to the GP trans-membrane domain.

Our data reveal the arrangement of VP40 in assembled filovirus particles. They are consistent with a model for filovirus assembly in which oligomerization of VP40 dimers into curved chains via CTD-CTD interactions at the plasma membrane induces local membrane curvature. Stacking of VP40 chains results in the formation of 2D lattices which are curved in one direction. Membrane curvature can be propagated over larger areas of the membrane by growth of patches of 2D lattice or by contact and “fusion” between neighbouring patches.

Acknowledgements.
The Briggs laboratory acknowledges financial support from the European Molecular Biology Laboratory, the Medical Research Council (MC_UP_1201/16) and the European Research Council (ERC) under the European Union's Horizon 2020 research and innovation programme (ERC-CoG-648432 MEMBRANEFUSION). The Becker group was supported by the Deutsche Forschungsgemeinschaft (Sonderforschungsbereich 1021) and by the German Center for Infection Research (DZIF). The Saphire group was supported by institutional funds of the La Jolla Institute for Immunology. We thank A. Tan for assistance with preliminary data processing, D.M. Abelson for assistance with mutagenesis and W. J. H. Hagen (EMBL Heidelberg) for assistance during tomographic data collection. The SSRL Structural Molecular Biology Program is

supported by the DOE Office of Biological and Environmental Research, and by the National Institutes of Health, National Institute of General Medical Sciences (including P41GM103393). The Advanced Photon Source is a U.S. Department of Energy (DOE) Office of Science User Facility operated for the DOE Office of Science by Argonne National Laboratory under Contract No. DE-AC02-06CH11357.

Materials and methods

Expression, crystallization and crystal structure determination of Ebola VP40

eVP40 was expressed in E. coli BL21 cells as previously described(Bornholdt et al., 2013) and crystallized in 100 mM HEPES, 50 mM MgCl2, 38% PEG400, pH 7.2. Crystals belonging to the $P6_2$ space group diffracted to 2.4 Å , at Beamline 12-2 of the Stanford Synchrotron Radiation Lightsource (SSRL). Crystals belonging to the space group $P6_422$ space group diffracted anisotropically to 3.7Å, at the Argonne National Laboratory, Beamline SBC- 19-ID. Data integration and scaling were performed using the autoPROC implementation of XDS and AIMLESS(Vonrhein et al., 2011). Anisotropy correction of the zVP40 $P6_422$ data set was performed using STARANISO with a surface threshold of $1.2/\sigma(I)$, implemented through the autoPROC pipeline(Vonrhein et al., 2018). Isotropic data were used for model building and refinement of the zVP40 $P6_2$ crystal form and anisotropic corrected data were used for model building and refinement of the zVP40 $P6_422$ crystal form. Both structures were determined using molecular replacement using PHENIX(Adams et al., 2010) with dimeric zVP40 (PDB: 4LDB) as the search model. Refinement of each crystal structure was done through iterative rounds of manual model building using COOT(Emsley et al., 2010), followed by refinement of the models in PHENIX.

Expression and purification of VLPs

HEK293T cells were transfected with the appropriate combination of full length plasmids in pCAGGS backbones: full-length Marburg virus VP40; Zaire Ebola virus VP40; Zaire Ebola virus VP40 and GP; or Zaire Ebola virus NP, VP24, VP35, and VP40(Hoenen et al., 2006; Wenigenrath et al., 2010). Supernatant was collected 3 days after transfection and clarified by centrifugation at 800*g* for 10 min at 4 °C. The remaining steps were performed at 4 °C. VLPs were pelleted through a 20% (w/v) sucrose cushion in TNE buffer (50 mm Tris–HCl pH 7.4, 100 mm NaCl, 0.1 mm EDTA) at 160,000*g* for 3 h, resuspended in TNE buffer, and separated on a Nycodenz step gradient (2.5%, 5%, 7.5%, 10%, 15%, 20%, 30% (v/v)) at 34,400*g* for 15 min. Fractions 4–6 were collected and checked by negative-stain EM; fractions confirmed to contain VLPs were pooled and pelleted at 92,000*g* for 2 h. Final pellets were resuspended in TNE.

VLP budding assay

Budding of virus-like particles (VLPs) into cell supernatants was detected by Western blot analyses. Wild-type and mutant VP40 bearing a Strep-Tag were cloned into pTriEx-5 (Novagen) and transfected into cells using TrasnIT-LT1 transfection reagent (Mirus). VLPs were harvested 24 h posttransfection. Cell culture medium was spun down at 3500 rpm for 20 min to pellet any cells out of the media. The cleared supernatants were then ultracentrifuged at 30,000 rpm

with an SW-60 rotor (Beckman) for 2 hrs through a 20% (w/v) sucrose cushion-50 mM Tris pH 7.4, 100 mM NaCl. Pelleted VLPs were resuspended in 1X NuPAGE LDS sample buffer (ThermoFisher). Cell lysates were collected by washing cells twice with PBS followed by lysis in CytoBuster. VLPs and cell lysates were then run on SDS denaturing gels, transferred onto polyvinylidene difluoride (PVDF) Immobilon transfer membranes (Millipore), and probed with an anti-Strep-Tag antibody (GeneTex). The relative intensities of the bands were quantified by densitometry with a ChemiDoc MP imaging system (Bio-Rad) and ImageJ. The budding index was defined as the amount of Strep-VP40 in the VLPs divided by the amount in the cell lysate and presented as % of wild-type Strep-VP40.

Preparation of inactivated Marburg virus

Virus specimens were grown, purified, and fixed under BSL-4 conditions as previously described(Bharat et al., 2011). Briefly, Huh7 cells were infected with Marburg virus. Supernatant was collected 1 day post infection, and centrifuged at 4 °C for 2 h at approximately 77,000g through a 20% (w/w) sucrose cushion to isolate the virus particles. The resultant virus pellet was resuspended in calcium and magnesium deficient phosphate-buffered saline (PBS), re-pelleted, and inactivated with paraformaldehyde in DMEM (final concentration 4%) for 24 h by filling the tube completely. The viruses were pelleted and the 4% paraformaldehyde solution in DMEM (w/v) was replaced with a fresh solution of 4% paraformaldehyde. The sample was released from the BSL-4 facility after an additional 24 h.

Cryo-electron tomography

C-Flat 2/2-3C grids stored under vacuum were glow discharged for 30 s at 20 mA. Virus or VLP solution was diluted with 10 nm colloidal gold; 2.5 µl of this mixture was applied to each grid and plunge frozen into liquid ethane using a FEI Vitrobot Mark 2. Grids were stored in liquid nitrogen until imaging. Tomographic imaging was performed as described previously(Schur et al., 2016; Wan et al., 2017). Briefly, imaging was performed on a FEI Titan Krios at 300 keV using a Gatan Quantum 967 LS energy filter with a slit width of 20 eV and a Gatan K2xp detector in super-resolution mode. Tomograms were acquired from −60° to 60° with 3° steps using SerialEM(Mastronarde, 2005) and a scripted dose-symmetric tilt-scheme(Hagen et al., n.d.). Data collection parameters are provided in **Table S2**.

Frames were aligned with either K2Align software, which uses the MotionCorr algorithm(Li et al., 2013), or with the frame alignment algorithm built into serialEM; aligned frames were Fourier cropped to 4k × 4k, giving a final pixel size of 1.78 Å per pixel. Defocus for each tilt was determined by CTFFIND4(Rohou and Grigorieff, n.d.). Tilt images were filtered by cumulative electron dose using the exposure-dependent attenuation function and critical exposure constants as described elsewhere(Schur et al., 2016). Contrast transfer functions (CTFs) of individual images were corrected using ctfphaseflip(Xiong et al., 2009) and tomograms were reconstructed using weighted back projection in IMOD(Kremer et al., 1996). Tomograms with poor fiducial alignment were discarded; poor fiducial alignment was defined as

alignment residual above one pixel in 2× binned data or retaining fewer than eight fiducial markers. CTF-corrected unbinned tomograms were binned by 2× (3.56 Å per pixel) and 4× (7.12 Å per pixel) by Fourier cropping.

Subtomogram Averaging

Filaments of interest were first identified in 4×-binned tomograms using Amira visualization software (FEI Visualization Sciences Group). Using Amira and the electron microscopy toolbox(Pruggnaller et al., 2008), points were selected along the central filament axes and radii were measured along the matrix layers. These were then used to define the filament axes and generate an oversampled cylindrical grid for each filament along the matrix layer. These gridpoints served as initial extraction points for subtomograms. Initial Euler angles for each gridpoint were derived from the cylindrical grid. These initial positions and orientations were used to generate the initial motivelist, the metadata file for subtomogram averaging.

Initial references were generated by subtomogram averaging of single filaments using 4× binned data. Subtomogram averaging was performed using TOM(Nickell et al., 2005), AV3(Förster et al., 2005) and dynamo(Castaño-Díez et al., 2012), and scripts derived from their functions. Using the initial motivelist, the initial average that was roughly a cylindrically averaged section of a filament. From there a six-dimensional search was performed to refine Euler angles and Cartesian shifts, resulting in a low-resolution structure.

At this point, it became clear that the matrix layer was not helical in structure and had C2 symmetry, indicating the structures were apolar with respect to the filament axis. As such, initial references for each speciment were used to align the full datasets using C2 symmetry. Initial alignments were performed using 4× binned data and a low pass filter limiting resolutions to 35 Å. After convergence of subunit positions, oversampled particles were removed by distance thresholding. Each tomogram was also thresholded by cross-correlation to exclude subtomograms that had misaligned to positions away from the matrix layer. The unique particle parameters were then split into 'odd and even' sets, and aligned independently from this point on. Subtomograms were re-extracted with 2× binning and halfsets were aligned independently until the six-dimensional search converged. This was then repeated with 1× binned data. Final resolutions were measured using a mask-corrected FSC(Chen et al., 2013), and final averages were low-pass filtered, sharpened, CTF-reweighted, and figure-of-merit weighted to their determined resolutions as previously described(Schur et al., 2016). Data processing parameters are provided in **Table S2**.

Visualization and rigid body fitting

Visualization of tomograms and electron density maps were done with University of California, San Francisco (UCSF) Chimera(Pettersen et al., 2004). Rigid body fitting of atomic models into density maps was performed using the fit-in-map function in UCSF Chimera.

Measuring 2D crystal lattices

Approximate 2D crystal lattices were measured from the subtomogram averages. Prior to measurement, the structures were 'unwrapped' from Cartesian space to cylindrical polar space, allowing for direct measurement along the cylindrical surface. Measurements were performed near the middle of the VP40 dimeric interface.

Lattice maps and neighbor density plots

The data for lattice maps are the positions and the orientations of the subtomograms determined during subtomogram averaging. Lattice maps were visualized in UCSF Chimera using the Place Objects plugin(Qu et al., 2018).

Neighbor density plots are calculated by first picking a reference subtomogram, then finding all neighbors within a given distance threshold. The reference subtomogram, along with its neighbors, is then shifted and rotated into the center of the density plot, and all neighbors are added to the plot. When performed across all subtomograms, the result is a set of point clouds that represent the probability of finding a neighboring subtomogram in those positions. The probability distributions of the point cloud should reflect the positions of subunits in the subtomogram averages, with neighbor density clouds becoming more dispersed away from the center of the plot, reflecting the loss of resolution away from the center of the average.

Cross-neighbour density maps are calculated using two motivelists, with one containing the reference subtomograms, and the other containing the orientations of the second proteins of interest.

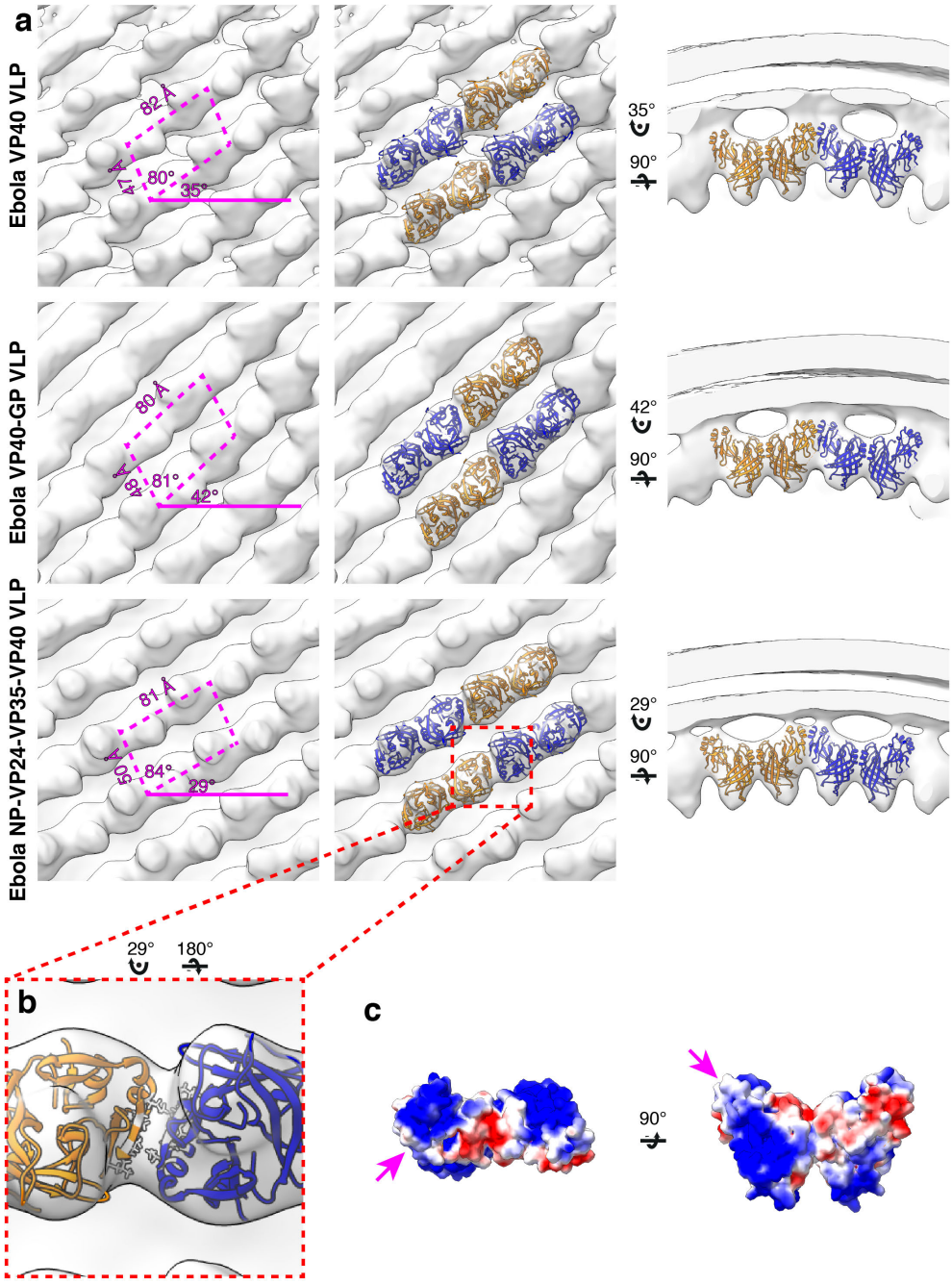

Figure 1: Subtomogram averages of the eVP40 matrix layer in VLPs. a) the structure of the matrix layer in Ebola VP40, VP40-GP, and NP-VP24-VP35-VP40 VLPs. For these rows, the left column shows a portion of the subtomogram average from within the VLP; overlaid are the approximate unit-cell dimensions of the 2D lattice. eVP40 dimers are fitted as rigid bodies in the central column (PDB: 4ldb). The right column shows a cross-sectional view parallel to a VP40 linear chain. **b)** A detailed view of the inter-dimeric CTD-CTD interface in Ebola NP-VP24-VP35-VP40 matrix, with hydrophobic residues at the inter-dimer interface shown in white; this interface is present in all three VLPs. **c)** Electrostatic maps of the eVP40 dimer, with the hydrophobic patch forming the inter-dimer interface marked by an arrowhead.

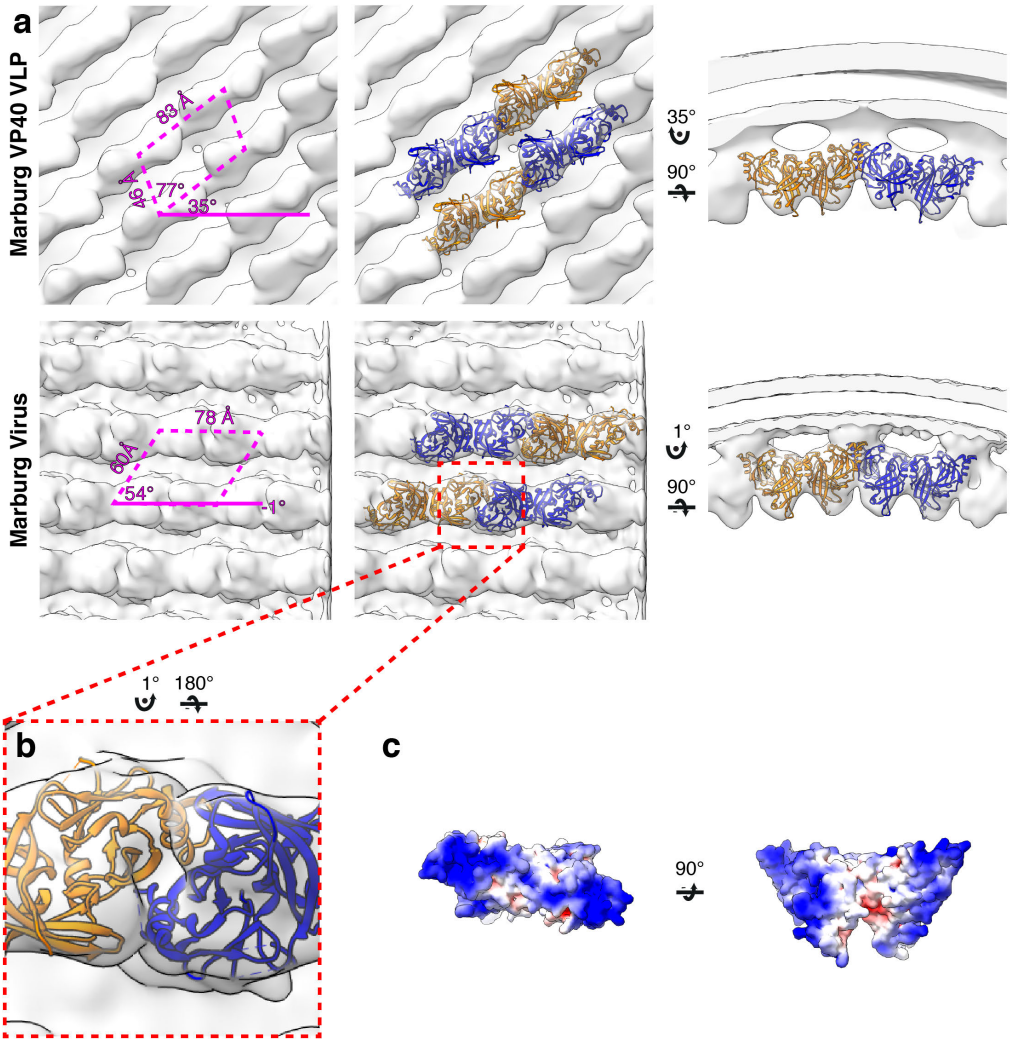

Figure 2: Subtomogram averages of the mVP40 matrix layer in VLPs and virions. a) top row shows the structure of the matrix layer in Marburg VP40 VLPs and bottom row shows Marburg virus. Left column shows a portion of the subtomogram average from within the filaments; overlaid are the approximate unit-cell dimensions of the 2D lattice. Center column shows the same view, but rigid-body fitted mVP40 dimers (PDB: 5b0v). Right column shows the same rigid-body fitting as in the center column, but as a cross-sectional view parallel to a VP40 linear chain. **b)** a detailed view of the inter-dimeric CTD-CTD interface. **c)** electrostatic maps of mVP40 dimer.

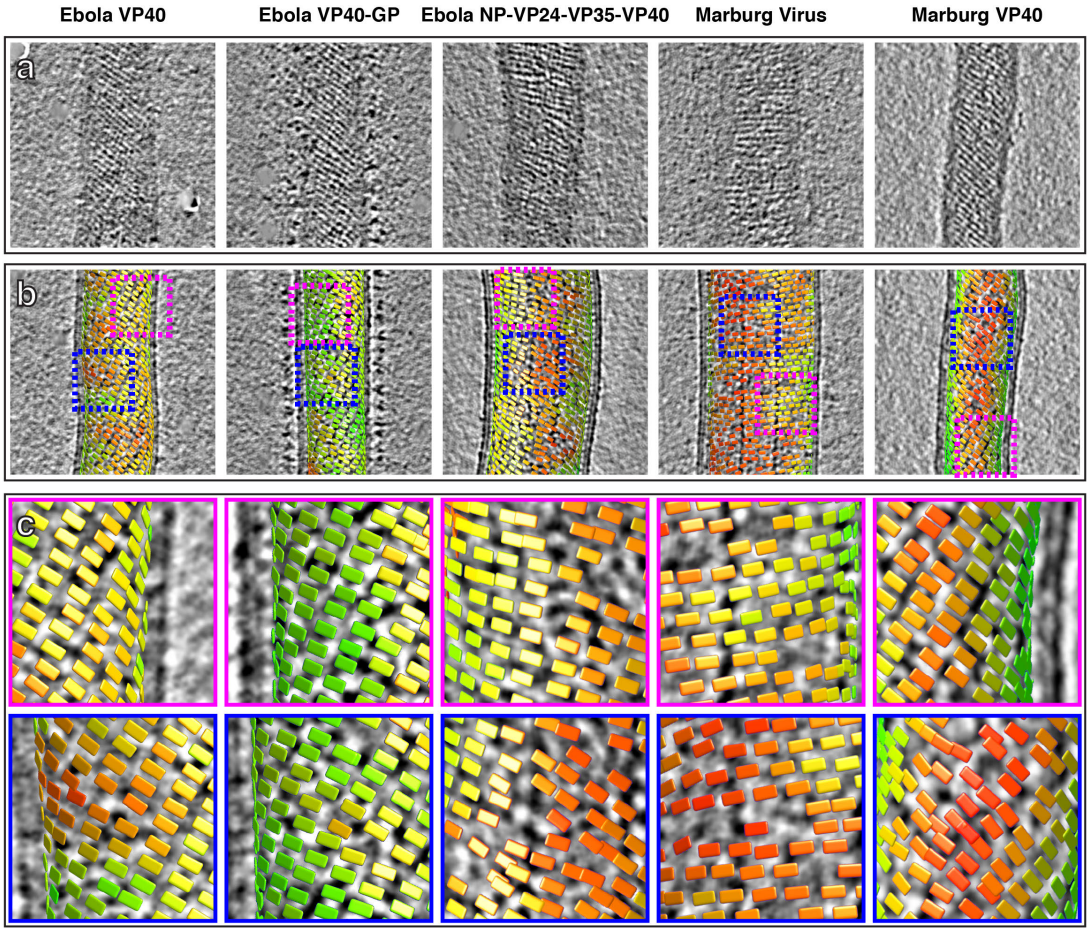

Figure 3: Tomographic slices and lattice maps of matrix layers. a) Tomographic slice of the matrix layer protein density directly under the membrane bilayer; VP40 chains are seen as dark lines of density. **b)** Central slice through each filament with lattice maps overlaid. VP40 dimers are visualized as rectangles, which connect into linear chains along the short sides. Colors are scaled from green to red, which denote high and low correlation scores, respectively. Low correlation scores are generally associated with regions where the local lattice is broken, thus correlating poorly with the strong lattice in the subtomogram average. Representative well-ordered regions are boxed in magenta, while representative poorly-ordered regions are boxed in blue. Both are shown in detail in **c**.

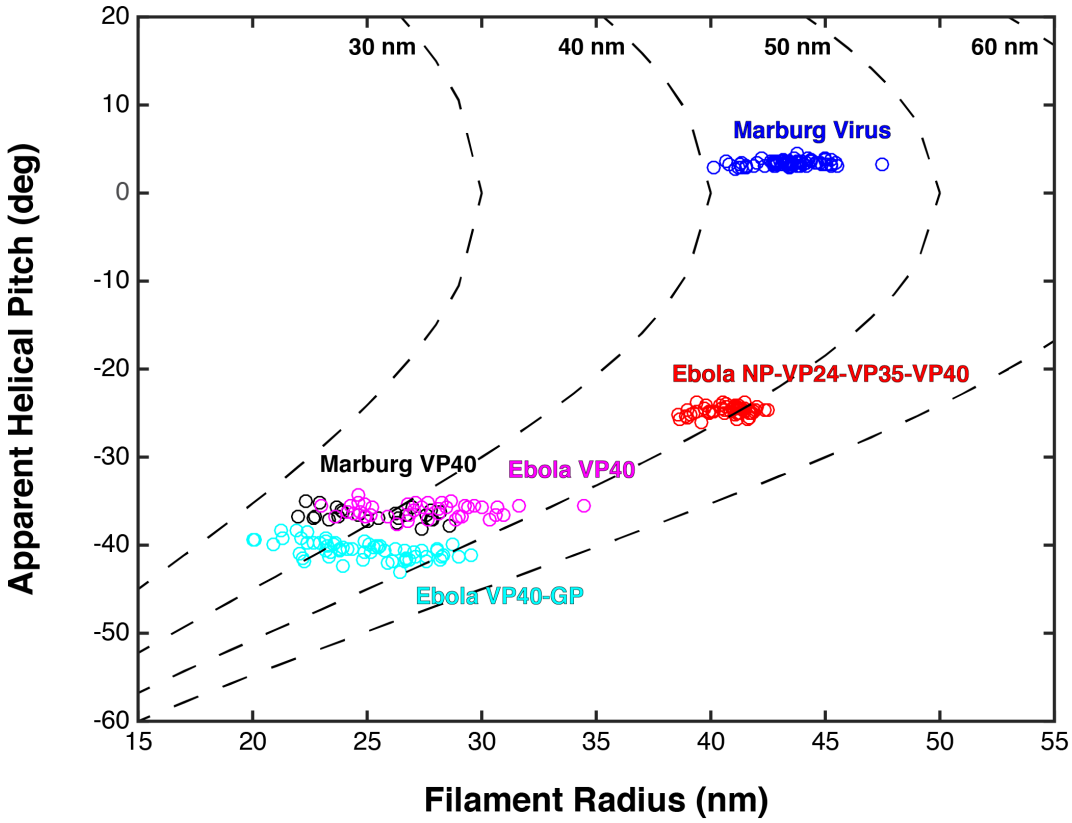

Figure 4: Plots of filament radii with respect to apparent helical pitch of linear VP40 chains. Scatter points represent measurements for individual filaments. Dotted lines represent expected helical pitch for given radius, assuming a constant radius of curvature. The radii of curvature plotted from left to right are 30, 40, 50, and 60 nm.

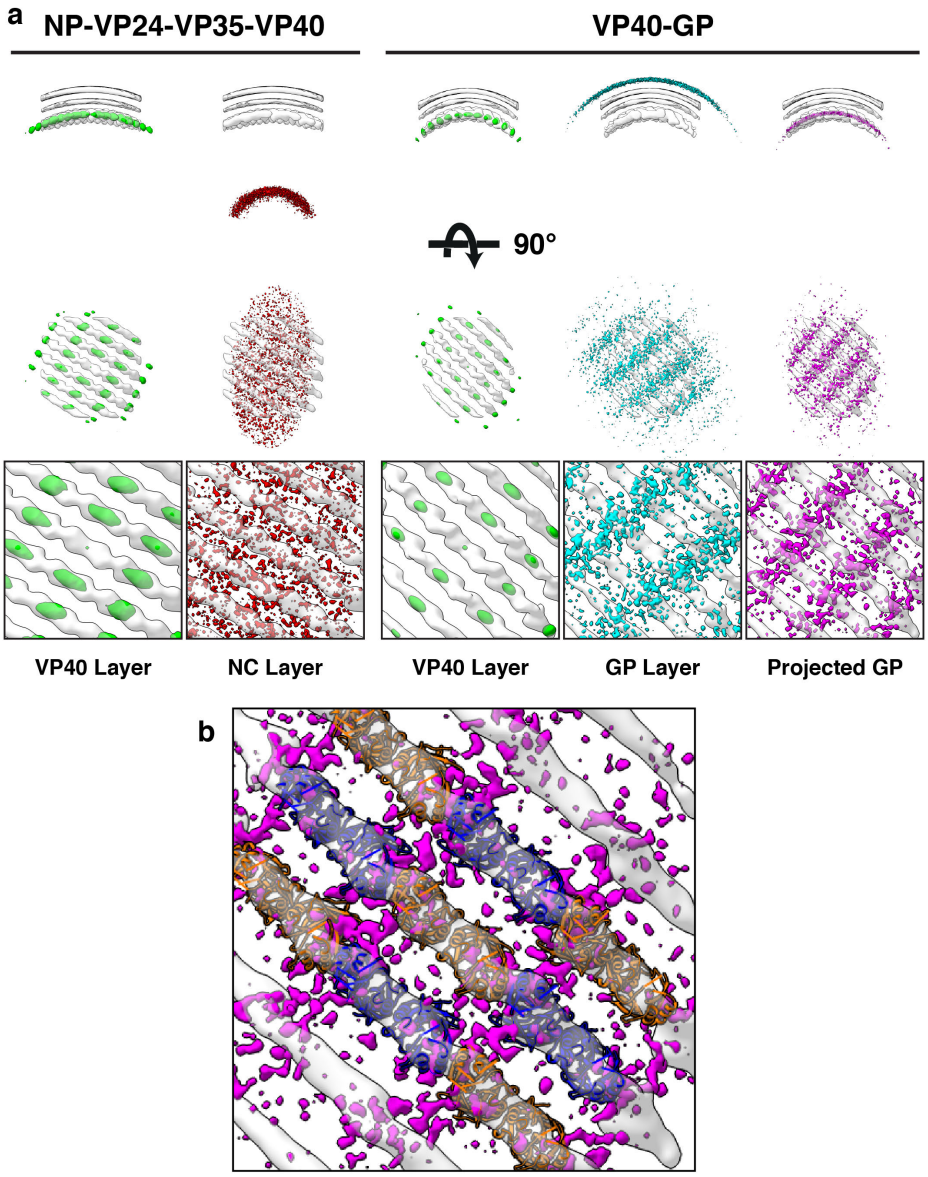

Figure 5: Neighbor density maps of Ebola VLPs. a) First two columns are from NP-VP24-VP35-VP40 VLPs while last three columns are from VP40-GP VLPs, respective subtomogram averaging structures are shown as transparent densities. Each neighbor density map is shown as a coloured isosurface indicating the preferred location of the named protein relative to the VP40 positions. Top row shows cross-sectional views through the filaments, center row shows view from outside the filaments, and bottom row shows detailed views from center row. In center and bottom rows, membrane is removed from subtomogram averages for easier viewing. The projected GP layer contains the same data as the GP layer, but projected on to the VP40 radius along the direction of the GP stalks. **b)** a zoomed-in view of the low projected GP panel, showing the preferred positions of GP relative to a model of the VP40 layer.

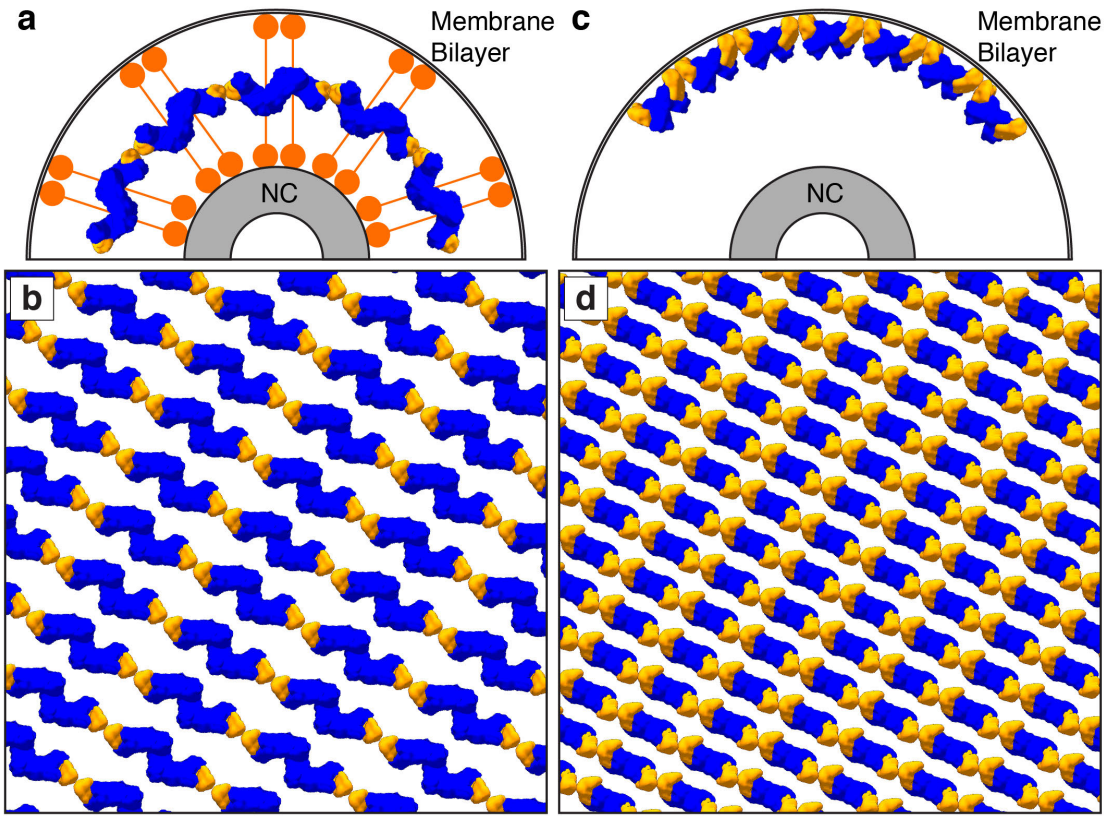

Figure 6: Comparison of linear hexamer and dimer-chain matrix models. VP40 NTDs are shown in blue and CTDs are shown in orange; orange circles represent the "sprung" CTDs of the linear hexamer. **a)** and **b)** show the linear hexamer model, where hexamers form a layer of density between the NC and membrane; the sprung CTDs tether the membrane bilayer to the NC. **a)** shows a cross-section view of the different layers, while **b)** shows a view through ordered matrix layer between the membrane and the NC. **c)** and **d)** shows our dimer-chain model, where VP40 dimers form linear chains directly below the membrane surface; an unknown non-VP40 component tethers the NC to the matrix layer. **c)** shows a cross-section view, while **d)** shows a surface view directly below the membrane surface.

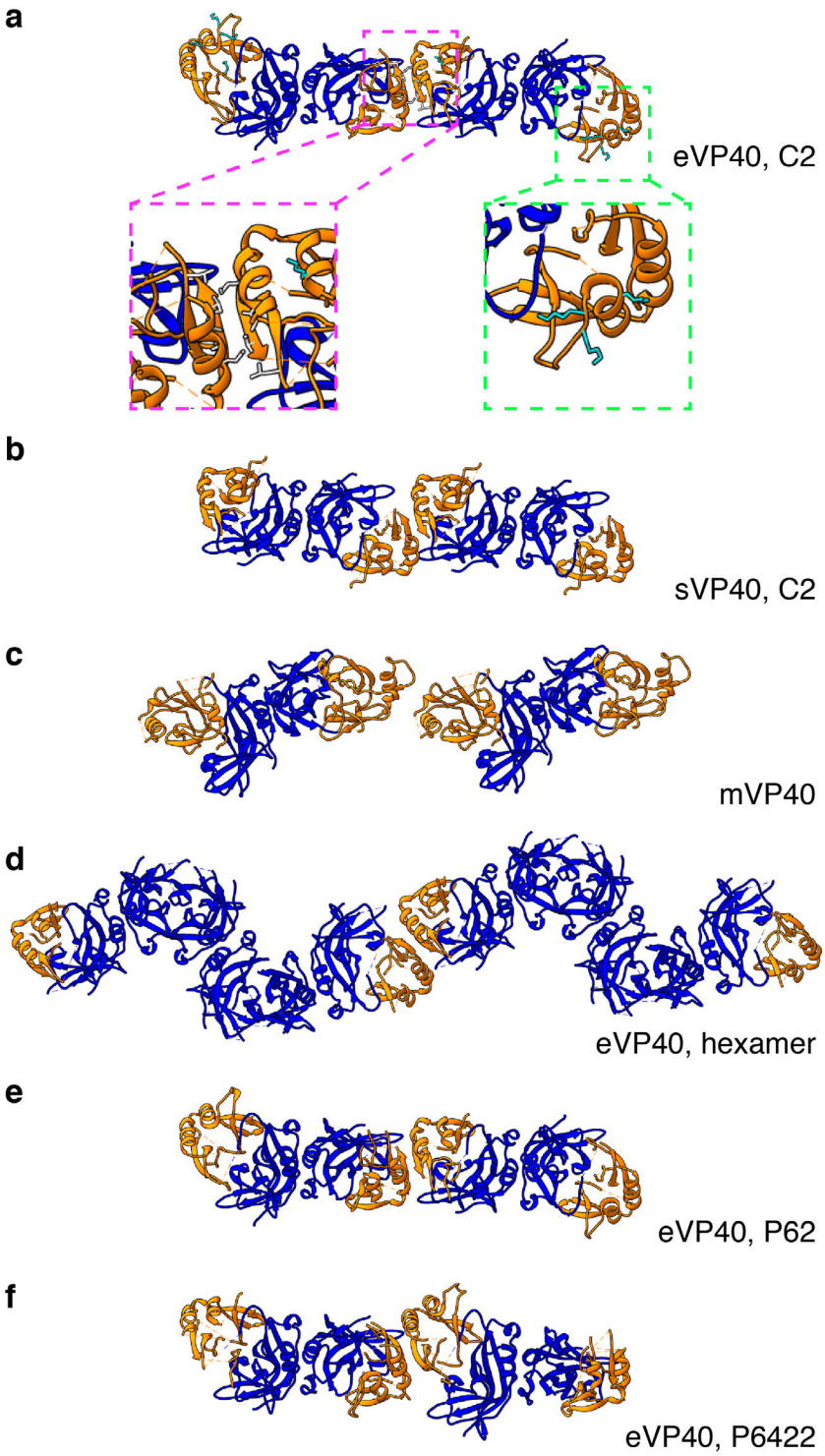

Figure S1: Comparison of eVP40 assembly models. Crystal structures of VP40 assembled by CTD-to-CTD interactions of VP40 dimers. NTDs are colored in blue, while CTDs are in orange. **a)** eVP40, C2, with insets showing the residues of the hydrophobic CTD-CTD interface (magenta) and the CTD basic patch (green). **b)** sVP40, C2; **c)** mVP40; **d)** eVP40 linear hexamer, **e)** eVP40, $P6_2$, **f)** eVP40, $P6_422$. Views are from outside the membrane surface.

693

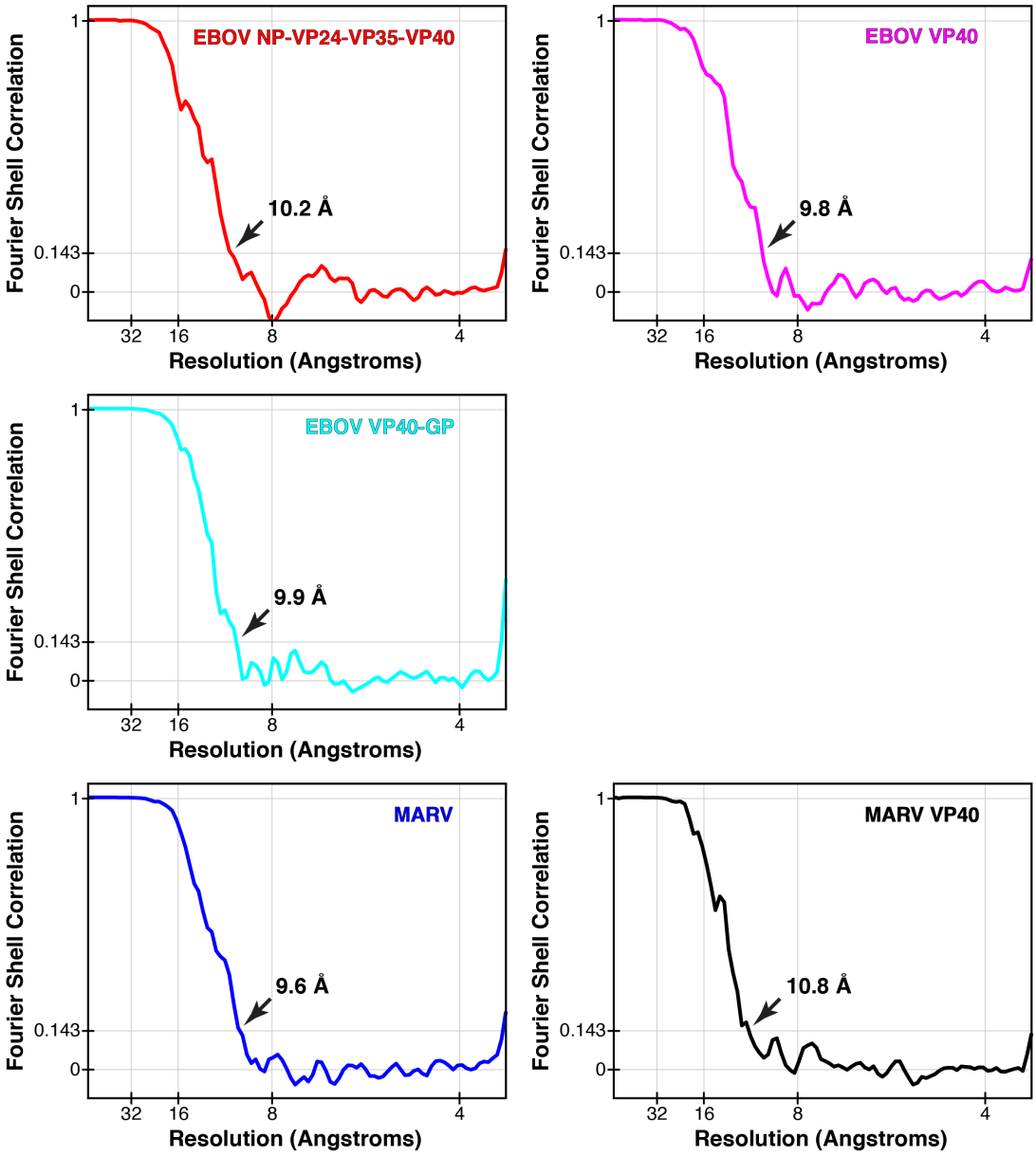

694
695

696 **Figure S2: Fourier shell correlations of each subtomogram average.** Arrows
697 indicate resolution at FSC = 0.143.

698
699

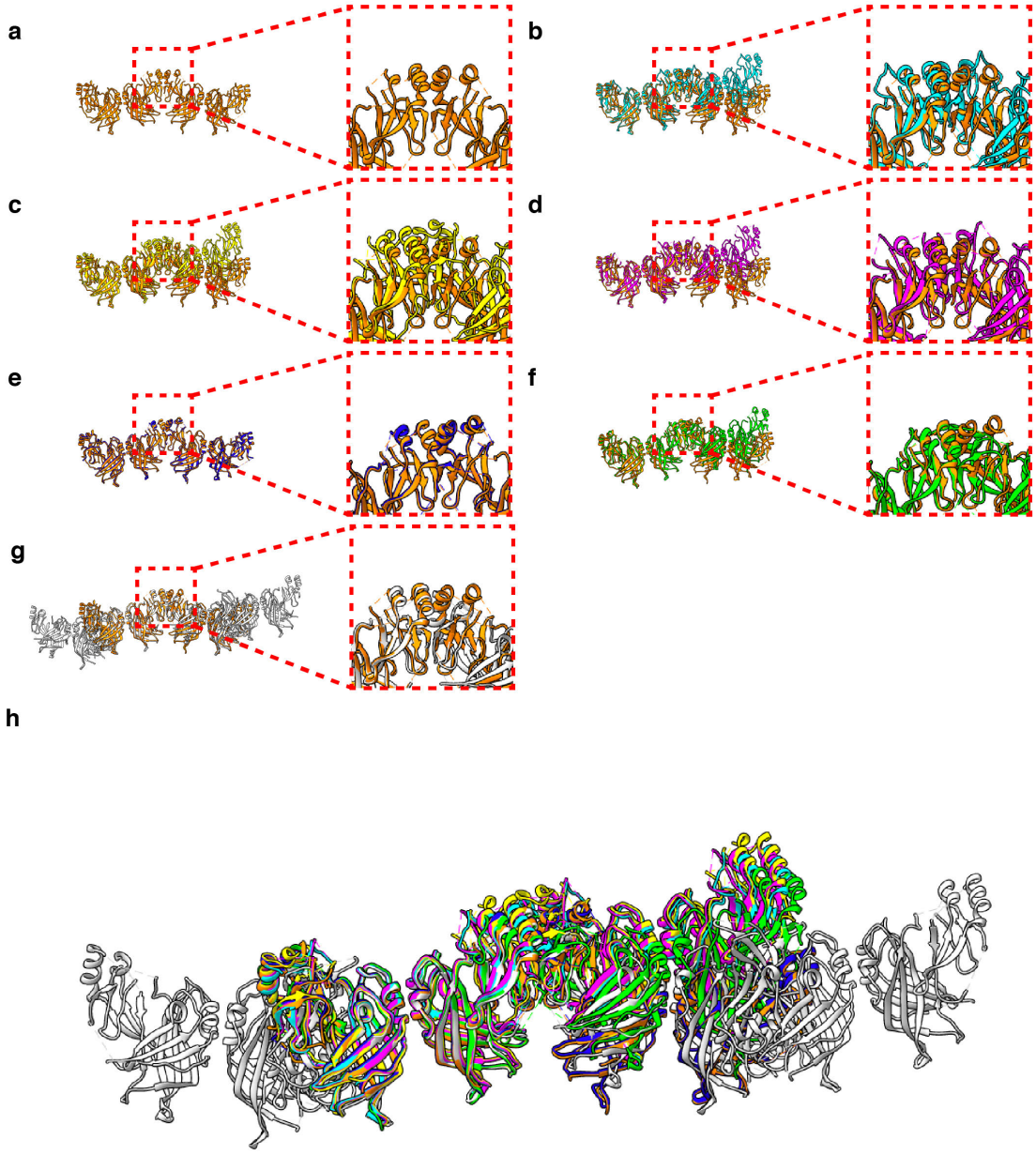

Figure S3. Comparison of crystal packings observed in eVP40 structures. a) Zaire eVP40 (4ldb(Bornholdt et al., 2013)) crystallographic dimer. This dimer is then shown overlaid with: **b)** Sudan eVP40 (3ctq(Bornholdt et al., 2013)), **c)** Zaire eVP40 (1es6(Dessen et al., 2000)) , **d)** Sudan eVP40 (4ld8(Bornholdt et al., 2013)), **e)** Zaire eVP40 $P6_2$ unit cell (this study), **f)** Zaire eVP40 $P6_422$ unit cell, (this study) **g)** Zaire eVP40 linear hexamer (4ldd(Bornholdt et al., 2013)), **h)** a superposition of all six structures.

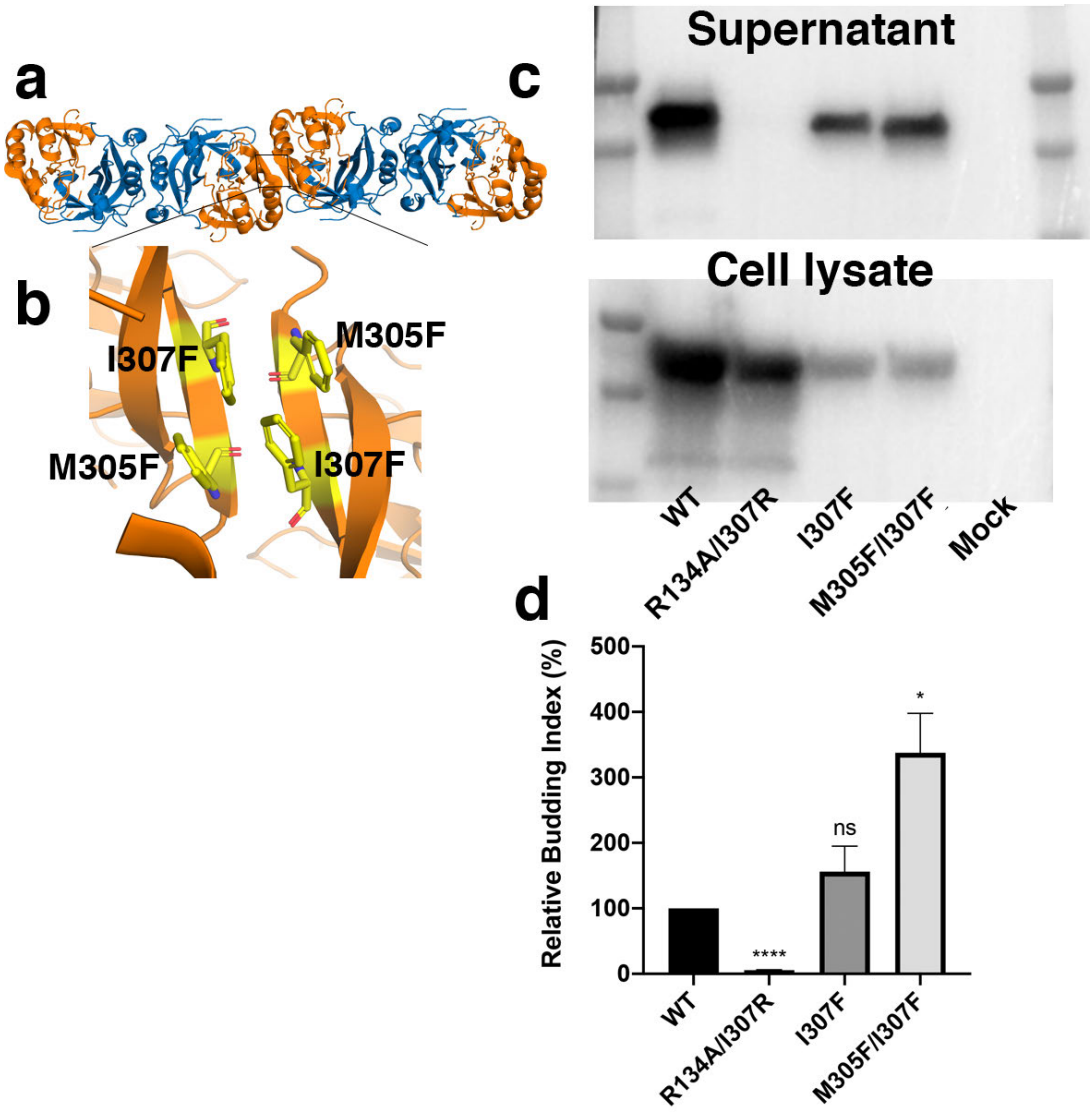

Figure S4. Characterization of mutations that stabilize the CTD-CTD interface. a) Structure of side-by-side VP40 dimers. NTDs are colored blue and CTDs are colored orange. **b)** Zoomed in view of the CTD-CTD interface. Modeling suggests that introduction of phenylalanine at positions 305 and 307 might stabilize the CTD-CTD interface. **c)** Expression level of wild-type, R134A/I307R, I307F, and I307F/M305F VP40. R134A/I307R has been previously described to abolish VP40 dimerisation and VLP release(Bornholdt et al., 2013), **d)** Relative budding index of VLPs into the supernatant (ratio of supernatant to cell-lysate VP40, normalized to the WT values) from WT and mutant VP40. Three independent replicates. Values represent mean +/- SEM ns = $P > 0.05$, *$P \leq 0.05$, ****$P \leq 0.0001$ by student's t test. The M305F/I307F mutation, predicted to stabilize the CTD-CTD interface, shows enhanced budding compared to WT VP40.

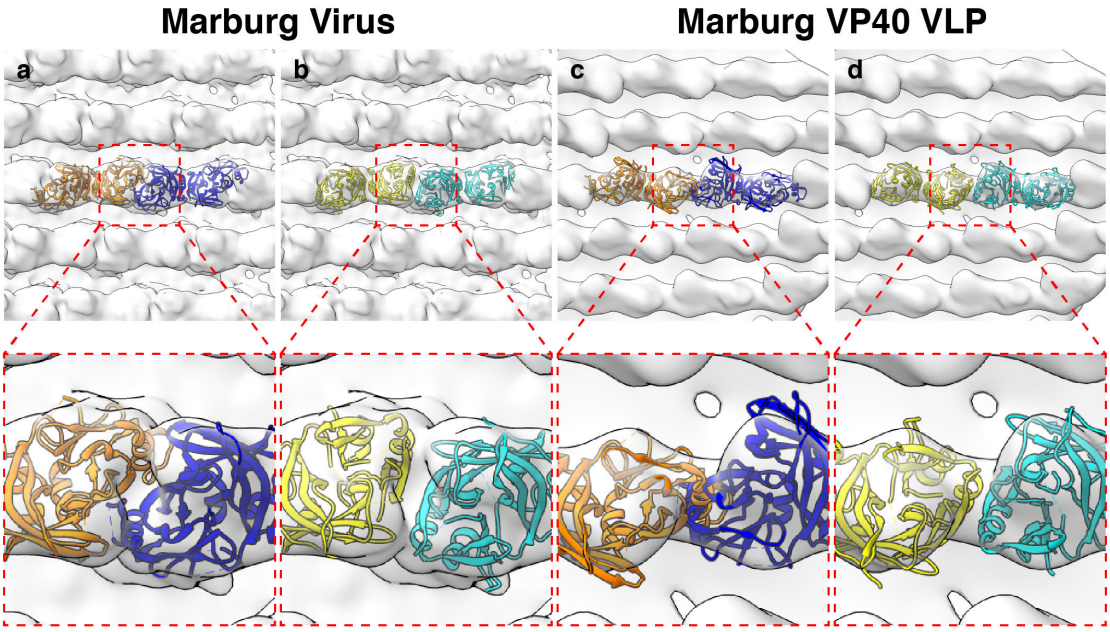

Figure S5. Rigid body fitting of crystal structures into mVP40 matrix layers. **a)** and **b)** are densities from Marburg virus while **c)** and **d)** are densities from mVP40 VLPs. mVP40 crystal structures (PDB: 5b0v) are in blue and orange while eVP40 structures (PDB: 4ldb) are in cyan and yellow. For Marburg virus, both structures fit without clashing, while in Marburg VP40 VLPs only the eVP40 structures fit, suggesting a conformational change between the mVP40 crystal structure and the VLP.

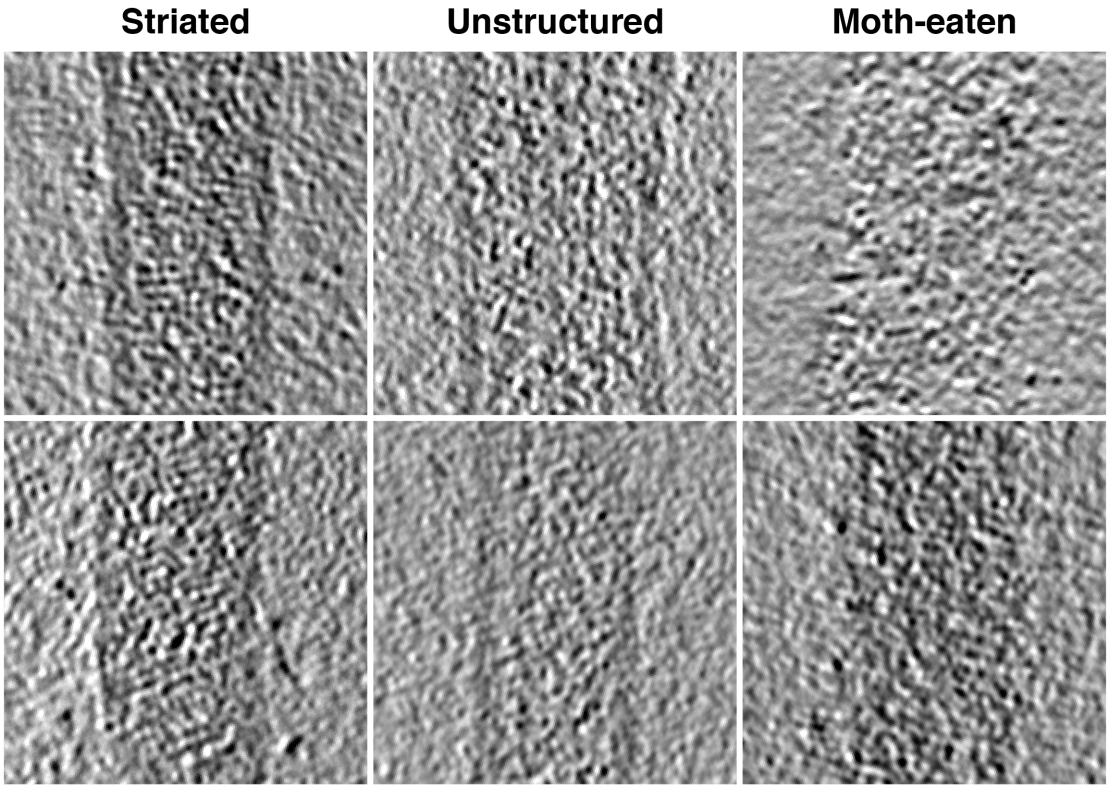

Figure S6: Tomographic slices of Ebola virus matrix layers. Left column shows regions that show ordered VP40 striations, center column shows virions with intact membranes but unstructured matrix layer, and right column shows matrix layer of moth-eaten membranes.

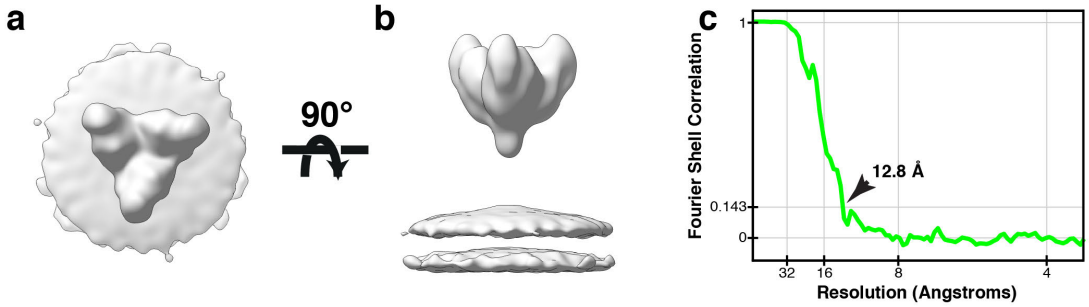

Figure S7: Structure of Ebola GP from eVP40-GP VLPs. a) Top and **b)** side view of Ebola GP subtomogram average. **c)** FSC plot of Ebola GP subtomogram average; arrow indicates resolution at FSC = 0.143.

Table 1: Unit cell and filament dimensions matrix layers.

Specimen	Radius (nm)	a (Å)	b (Å)	θ (°)	α (°)
Ebola VP40 VLPs	28±6 (n = 42)	82	47	80	35
Ebola VP40-GP VLPs	25±3 (n = 60)	80	48	81	42
Ebola NP-VP24-VP35-VP40 VLPs	41±2 (n = 54)	81	50	84	29
Marburg Virus	43±2 (n = 75)	78	60	54	-1
Marburg VP40 VLPs	25±2 (n = 25)	83	46	77	35

Unit cell dimensions are illustrated in Figures 1 and 2 and are defined as follows: a is the distance between VP40 dimers along the chains, b is the distance between dimers between chains, θ is the internal angle of the lattice, and α is the rotational angle of the unit cell.

Table S1: Crystallographic data collection and refinement statistics

	zVP40 $P6_2$	**zVP40 $P6_422$**
Data Collection		
Space Group	$P6_2$	$P6_422$
Unit cell dimensions		
a, b, c (Å)	159.94, 159.94, 89.75	105.28, 105.28, 463.74
α, β, γ (°)	90, 90, 120	90, 90, 120
Wavelength (Å)	0.9795	0.9793
Resolution range (Å)[a]	45.22 - 2.46 (2.55 - 2.46)	19.87 – 4.78 (4.86 – 4.78)
Observations[a]	352162 (38027)	95505 (4826)
Unique Reflections[a]	44322 (4321)	8087 (373)
Completeness (%)[a]	91.74 (91.08)	99.6 (100)
Redundancy[a]	7.9 (8.0)	11.8 (12.9)
$CC_{1/2}$[a]	0.998 (0.463)	0.99 (0.97)
$\langle I/\sigma I \rangle$[a]	16.66 (0.90)	11.0 (2.3)
R_{merge}[a]	0.09958 (3.476)	0.117 (1.234)
R_{pim}[a]	0.03766 (1.301)	0.045 (0.470)
Anisotropy Correction		
Anisotropic resolution (Å)		5.54 (0.89 a* - 0.45 b*)
(direction)		5.54 b*
		3.60 c*
Resolution after correction[a]		19.88 – 3.77 (4.30 – 3.77)
No. of unique reflections[a] (ellipsoidal)		7430 (372)
$\langle I/\sigma I \rangle$ (ellipsoidal)[a]		12.3 (1.6)
Completeness (ellipsoidal) (%)[a]		90.9 (65.9)
Refinement		
No. Atoms	7730	7143
R_{cryst}/R_{free} (%)	20.89/26.15	28.93/32.27
Ramachadran plot		
Outliers (%)	0.62	0.23
Allowed (%)	6.22	3.98
Favored (%)	93.16	95.80
RMSD from ideal geometry		
Bond length (Å)	0.011	0.005
Bond angles (°)	1.53	1.02
Clashscore	14.8	8.78
Average B Factor	92.77	169.84
Refinement Program	Phenix	Phenix

[a]Numbers in parentheses correspond to the outer resolution shell.

Table S2: Data collection and image processing table.

	EBOV NP-VP24-VP35-VP40	EBOV VP40	EBOV VP40-GP	MARV	MARV VP40
Magnification	81,000x	81,000x	81,000x	81,000x	81,000x
Voltage (kV)	300	300	300	300	300
Electron exposure (e-/ Å^2)	~100	~100	~100	~80	~100
Defocus range (μm)	-2.0 to -4.5	-2.0 to -4.5	-2.0 to -4.5	-2.0 to -4.5	-2.0 to -4.5
Detector	Gatan Quantum K2	Gatan Quantum K2	Gatan Quantum K2	Gatan Quantum K2	Gatan Quantum K2
Energy Filter	Yes	Yes	Yes	Yes	Yes
Slit Width (eV)	20	20	20	20	20
Tilt Range (min/max, step)	-60°/60°, 3°	-60°/60°, 3°	-60°/60°, 3°	-60°/60°, 3°	-60°/60°, 3°
Pixel Size (Å)	1.78	1.78	1.78	1.78	1.78
Tomograms (used/acquired)	52/64	39/42	55/73	76/82	34/35
Filaments	54	43	65	93	34
Symmetry	C2	C2	C2	C2	C2
Final Subtomograms (no.)	59580	20352	106793	75212	42938
Map Resolutions (FSC = 0.143)	10.2 Å	9.8 Å	9.9 Å	9.6 Å	10.8 Å

References

Adams PD, Afonine PV, Bunkóczi G, Chen VB, Davis IW, Echols N, Headd JJ, Hung L-W, Kapral GJ, Grosse-Kunstleve RW, McCoy AJ, Moriarty NW, Oeffner R, Read RJ, Richardson DC, Richardson JS, Terwilliger TC, Zwart PH. 2010. PHENIX: a comprehensive Python-based system for macromolecular structure solution. *Acta Crystallogr D Biol Crystallogr* **66**:213–221. doi:10.1107/S0907444909052925

Beniac DR, Melito PL, deVarennes SL, Hiebert SL, Rabb MJ, Lamboo LL, Jones SM, Booth TF. 2012. The Organisation of Ebola Virus Reveals a Capacity for Extensive, Modular Polyploidy. *PLoS ONE* **7**:e29608. doi:10.1371/journal.pone.0029608

Bharat TAM, Noda T, Riches JD, Kraehling V, Kolesnikova L, Becker S, Kawaoka Y, Briggs JAG. 2012. Structural dissection of Ebola virus and its assembly determinants using cryo-electron tomography. *Proc Natl Acad Sci* 201120453. doi:10.1073/pnas.1120453109

Bharat TAM, Riches JD, Kolesnikova L, Welsch S, Krähling V, Davey N, Parsy M-L, Becker S, Briggs JAG. 2011. Cryo-Electron Tomography of Marburg Virus Particles and Their Morphogenesis within Infected Cells. *PLoS Biol* **9**:e1001196. doi:10.1371/journal.pbio.1001196

Bornholdt ZA, Noda T, Abelson DM, Halfmann P, Wood MR, Kawaoka Y, Saphire EO. 2013. Structural Rearrangement of Ebola Virus VP40 Begets Multiple Functions in the Virus Life Cycle. *Cell* **154**:763–774. doi:10.1016/j.cell.2013.07.015

Castaño-Díez D, Kudryashev M, Arheit M, Stahlberg H. 2012. Dynamo: A flexible, user-friendly development tool for subtomogram averaging of cryo-EM data in high-performance computing environments. *J Struct Biol*, Special Issue: Electron Tomography **178**:139–151. doi:10.1016/j.jsb.2011.12.017

Chen S, McMullan G, Faruqi AR, Murshudov GN, Short JM, Scheres SHW, Henderson R. 2013. High-resolution noise substitution to measure overfitting and validate resolution in 3D structure determination by single particle electron cryomicroscopy. *Ultramicroscopy* **135**:24–35. doi:10.1016/j.ultramic.2013.06.004

Clifton MC, Bruhn JF, Atkins K, Webb TL, Baydo RO, Raymond A, Lorimer DD, Edwards TE, Myler PJ, Saphire EO. 2015. High-resolution Crystal Structure of Dimeric VP40 From Sudan ebolavirus. *J Infect Dis*. doi:10.1093/infdis/jiv090

Dessen A, Volchkov V, Dolnik O, Klenk H-D, Weissenhorn W. 2000. Crystal structure of the matrix protein VP40 from Ebola virus. *EMBO J* **19**:4228–4236. doi:10.1093/emboj/19.16.4228

Emsley P, Lohkamp B, Scott WG, Cowtan K. 2010. Features and development of Coot. *Acta Crystallogr D Biol Crystallogr* **66**:486–501. doi:10.1107/S0907444910007493

Feldmann H, Sanchez A, Geisbert TW. 2013. Filoviridae: Marburg and Ebola viruses. *Fields Virol 6th Ed Phila Lippincott Williams Wilkins* 923–56.

Förster F, Medalia O, Zauberman N, Baumeister W, Fass D. 2005. Retrovirus envelope protein complex structure in situ studied by cryo-electron tomography. *Proc Natl Acad Sci U S A* **102**:4729–4734. doi:10.1073/pnas.0409178102

826 Geisbert TW, Jahrling PB. 1995. Differentiation of filoviruses by electron
827 microscopy. *Virus Res* **39**:129–150. doi:10.1016/0168-1702(95)00080-1
828 Gomis-Rüth FX, Dessen A, Timmins J, Bracher A, Kolesnikowa L, Becker S, Klenk
829 H-D, Weissenhorn W. 2003. The Matrix Protein VP40 from Ebola Virus
830 Octamerizes into Pore-like Structures with Specific RNA Binding
831 Properties. *Structure* **11**:423–433. doi:10.1016/S0969-2126(03)00050-9
832 Hagen WJH, Wan W, Briggs JAG. n.d. Implementation of a cryo-electron
833 tomography tilt-scheme optimized for high resolution subtomogram
834 averaging. *J Struct Biol*. doi:10.1016/j.jsb.2016.06.007
835 Harty RN, Brown ME, Wang G, Huibregtse J, Hayes FP. 2000. A PPxY motif within
836 the VP40 protein of Ebola virus interacts physically and functionally with
837 a ubiquitin ligase: Implications for filovirus budding. *Proc Natl Acad Sci*
838 **97**:13871–13876. doi:10.1073/pnas.250277297
839 Hoenen T, Biedenkopf N, Zielecki F, Jung S, Groseth A, Feldmann H, Becker S.
840 2010a. Oligomerization of Ebola Virus VP40 Is Essential for Particle
841 Morphogenesis and Regulation of Viral Transcription. *J Virol* **84**:7053–
842 7063. doi:10.1128/JVI.00737-10
843 Hoenen T, Groseth A, Kolesnikova L, Theriault S, Ebihara H, Hartlieb B, Bamberg
844 S, Feldmann H, Ströher U, Becker S. 2006. Infection of Naïve Target Cells
845 with Virus-Like Particles: Implications for the Function of Ebola Virus
846 VP24. *J Virol* **80**:7260–7264. doi:10.1128/JVI.00051-06
847 Hoenen T, Jung S, Herwig A, Groseth A, Becker S. 2010b. Both matrix proteins of
848 Ebola virus contribute to the regulation of viral genome replication and
849 transcription. *Virology* **403**:56–66. doi:10.1016/j.virol.2010.04.002
850 Hoenen T, Volchkov V, Kolesnikova L, Mittler E, Timmins J, Ottmann M, Reynard
851 O, Becker S, Weissenhorn W. 2005. VP40 Octamers Are Essential for Ebola
852 Virus Replication. *J Virol* **79**:1898–1905. doi:10.1128/JVI.79.3.1898-
853 1905.2005
854 Huang Y, Xu L, Sun Y, Nabel GJ. 2002. The Assembly of Ebola Virus Nucleocapsid
855 Requires Virion-Associated Proteins 35 and 24 and Posttranslational
856 Modification of Nucleoprotein. *Mol Cell* **10**:307–316. doi:10.1016/S1097-
857 2765(02)00588-9
858 Jasenosky LD, Neumann G, Lukashevich I, Kawaoka Y. 2001. Ebola Virus VP40-
859 Induced Particle Formation and Association with the Lipid Bilayer. *J Virol*
860 **75**:5205–5214. doi:10.1128/JVI.75.11.5205-5214.2001
861 Koehler A, Pfeiffer S, Kolesnikova L, Becker S. 2018. Analysis of the
862 multifunctionality of Marburg virus VP40. *J Gen Virol* **99**:1614–1620.
863 doi:10.1099/jgv.0.001169
864 Kolesnikova L, Bohil AB, Cheney RE, Becker S. 2007a. Budding of Marburgvirus is
865 associated with filopodia. *Cell Microbiol* **9**:939–951. doi:10.1111/j.1462-
866 5822.2006.00842.x
867 Kolesnikova L, Ryabchikova E, Shestopalov A, Becker S. 2007b. Basolateral
868 Budding of Marburg Virus: VP40 Retargets Viral Glycoprotein GP to the
869 Basolateral Surface. *J Infect Dis* **196**:S232–S236. doi:10.1086/520584
870 Kremer JR, Mastronarde DN, McIntosh JR. 1996. Computer Visualization of
871 Three-Dimensional Image Data Using IMOD. *J Struct Biol* **116**:71–76.
872 doi:10.1006/jsbi.1996.0013
873 Li X, Mooney P, Zheng S, Booth C, Braunfeld MB, Gubbens S, Agard DA, Cheng Y.
874 2013. Electron counting and beam-induced motion correction enable near

875 atomic resolution single particle cryoEM. *Nat Methods* **10**:584–590.
876 doi:10.1038/nmeth.2472
877 Licata JM, Johnson RF, Han Z, Harty RN. 2004. Contribution of Ebola Virus
878 Glycoprotein, Nucleoprotein, and VP24 to Budding of VP40 Virus-Like
879 Particles. *J Virol* **78**:7344–7351. doi:10.1128/JVI.78.14.7344-7351.2004
880 Mastronarde DN. 2005. Automated electron microscope tomography using
881 robust prediction of specimen movements. *J Struct Biol* **152**:36–51.
882 doi:10.1016/j.jsb.2005.07.007
883 Nickell S, Förster F, Linaroudis A, Net WD, Beck F, Hegerl R, Baumeister W,
884 Plitzko JM. 2005. TOM software toolbox: acquisition and analysis for
885 electron tomography. *J Struct Biol* **149**:227–234.
886 doi:10.1016/j.jsb.2004.10.006
887 Noda T, Aoyama K, Sagara H, Kida H, Kawaoka Y. 2005. Nucleocapsid-like
888 Structures of Ebola Virus Reconstructed Using Electron Tomography. *J Vet*
889 *Med Sci* **67**:325–328. doi:10.1292/jvms.67.325
890 Noda T, Hagiwara K, Sagara H, Kawaoka Y. 2010. Characterization of the Ebola
891 virus nucleoprotein–RNA complex. *J Gen Virol* **91**:1478–1483.
892 doi:10.1099/vir.0.019794-0
893 Noda T, Sagara H, Suzuki E, Takada A, Kida H, Kawaoka Y. 2002. Ebola Virus
894 VP40 Drives the Formation of Virus-Like Filamentous Particles Along
895 with GP. *J Virol* **76**:4855–4865. doi:10.1128/JVI.76.10.4855-4865.2002
896 Oda S, Noda T, Wijesinghe KJ, Halfmann P, Bornholdt ZA, Abelson DM, Armbrust
897 T, Stahelin RV, Kawaoka Y, Saphire EO. 2016. Crystal Structure of Marburg
898 Virus VP40 Reveals a Broad, Basic Patch for Matrix Assembly and a
899 Requirement of the N-Terminal Domain for Immunosuppression. *J Virol*
900 **90**:1839–1848. doi:10.1128/JVI.01597-15
901 Pettersen EF, Goddard TD, Huang CC, Couch GS, Greenblatt DM, Meng EC, Ferrin
902 TE. 2004. UCSF Chimera--a visualization system for exploratory research
903 and analysis. *J Comput Chem* **25**:1605–1612. doi:10.1002/jcc.20084
904 Pruggnaller S, Mayr M, Frangakis AS. 2008. A visualization and segmentation
905 toolbox for electron microscopy. *J Struct Biol* **164**:161–165.
906 doi:10.1016/j.jsb.2008.05.003
907 Qu K, Glass B, Doležal M, Schur FKM, Murciano B, Rein A, Rumlová M, Ruml T,
908 Kräusslich H-G, Briggs JAG. 2018. Structure and architecture of immature
909 and mature murine leukemia virus capsids. *Proc Natl Acad Sci*
910 **115**:E11751–E11760. doi:10.1073/pnas.1811580115
911 Rohou A, Grigorieff N. n.d. CTFFIND4: Fast and accurate defocus estimation from
912 electron micrographs. *J Struct Biol*. doi:10.1016/j.jsb.2015.08.008
913 Schur FKM, Obr M, Hagen WJH, Wan W, Jakobi AJ, Kirkpatrick JM, Sachse C,
914 Kräusslich H-G, Briggs JAG. 2016. An atomic model of HIV-1 capsid-SP1
915 reveals structures regulating assembly and maturation. *Science* **353**:506–
916 508. doi:10.1126/science.aaf9620
917 Timmins J, Scianimanico S, Schoehn G, Weissenhorn W. 2001. Vesicular Release
918 of Ebola Virus Matrix Protein VP40. *Virology* **283**:1–6.
919 doi:10.1006/viro.2001.0860
920 Vonrhein C, Flensburg C, Keller P, Sharff A, Smart O, Paciorek W, Womack T,
921 Bricogne G. 2011. Data processing and analysis with the autoPROC
922 toolbox. *Acta Crystallogr D Biol Crystallogr* **67**:293–302.
923 doi:10.1107/S0907444911007773

924 Vonrhein C, Tickle IJ, Flensburg C, Keller P, Paciorek W, Sharff A. 2018. Advances
925 in automated data analysis and processing within autoPROC, combined
926 with improved characterisation, mitigation and visualisation of the
927 anisotropy of diffraction limits using STARANISO.
928 Wan W, Kolesnikova L, Clarke M, Koehler A, Noda T, Becker S, Briggs JAG. 2017.
929 Structure and assembly of the Ebola virus nucleocapsid. *Nature* **551**:394.
930 Welsch S, Kolesnikova L, Krähling V, Riches JD, Becker S, Briggs JAG. 2010.
931 Electron Tomography Reveals the Steps in Filovirus Budding. *PLoS Pathog*
932 **6**:e1000875. doi:10.1371/journal.ppat.1000875
933 Wenigenrath J, Kolesnikova L, Hoenen T, Mittler E, Becker S. 2010. Establishment
934 and application of an infectious virus-like particle system for Marburg
935 virus. *J Gen Virol* **91**:1325–1334. doi:10.1099/vir.0.018226-0
936 Xiong Q, Morphew MK, Schwartz CL, Hoenger AH, Mastronarde DN. 2009. CTF
937 determination and correction for low dose tomographic tilt series. *J Struct*
938 *Biol* **168**:378–387. doi:10.1016/j.jsb.2009.08.016
939